Ratchet Effect in Partially Gated Multifinger Field-Effect Transistors

G. Rupper, S. Rudin, and M. S. Shur

Phys. Rev. Applied **9**, 064007 — Published 8 June 2018

DOI: 10.1103/PhysRevApplied.9.064007

Ratchet Effect in Partially Gated Field Effect Multi-Finger Transistors

G. Rupper and S. Rudin
U.S. Army Research Laboratory, 2800 Powder Mill Road, Adelphi, Maryland 20783, USA

M. S. Shur
Rensselaer Polytechnic Institute
Troy, NY, USA

ABSTRACT

The hydrodynamic simulations of the sub-THz and THz response in ratchet field effect structure with several gate fingers reveal a significant responsivity enhancement compared to similar non-ratchet structures. In high mobility structures, the response exhibits a plasmonic peak with half width determined by impurity and phonon scattering and by the viscosity of the electronic fluid. The device with a feature size of 100 nm exhibits a reasonable response up to 8 THz. At high frequencies, high mobilities, and short feature sizes (on the order of 50 nm) the viscosity of the two-dimensional (2D) electronic fluid becomes a dominant attenuation mechanism. The finite ratchet structures also exhibit plasmonic peaks at lower plasmonic frequencies corresponding to the wavelengths determined by the overall length of the structures. These results are important for the modeling, design, and optimization of highly sensitive sub-THz and THz ratchet plasmonic devices.

INTRODUCTION

The resurgence of interest in the THz electronic technology applications in communications[1, 2, 3], medicine and biotechnology [4, 5], VLSI testing [6, 7], defect identification [8], homeland security [9] and imaging [10] stimulated research on more efficient THz electronic detectors and sources. [11, 12] The multi-finger devices that can capture more of an impinging THz beam[13,14,15,16, 17] and allow for an efficient coupling of the THz electric field are of special interest. Recently, the multi finger ratchet THz detector structures[18,19, 20] have attracted a lot of attention. These structures incorporate the spatial phase shift between the periodically modulated steady state channel potential and the impinging THz field pattern. Such periodic break in the structure symmetry leads to a large enhancement in the device responsivity and to the appearance of resonant plasmonic peaks in the photovoltaic response to the THz radiation. [18] The circularly or elliptically polarized THz radiation induces the rectified lateral current flowing in the direction along the gate fingers also exhibiting a resonant plasmonic peak in high mobility structures. [18]

We now report on the hydrodynamic simulations of the sub-THz and THz response in ratchet field effect structures with a finite number (six) gate fingers (see Fig. 1). The potential modulation in the two-dimensional electron gas could be achieved by periodic doping varying the local threshold voltage as shown in the Fig. 1(a). The resulting electron density distributions are shown in the same Fig. 1(b) for different values of the shift between doping profile and gate structure. Fig. 2 shows the biasing arrangements used in the simulation. The biasing scheme in Fig. 1(a) is for a general case of two different AC voltages at the source and gate contacts. The biasing arrangement in Fig. 2(b) corresponds to the THz voltage induced between the source and

gate with the open drain circuit. The terahertz current flowing between the gate and source flows in the device channel being rectified due to the device nonlinearities leading to the induced DC voltage drop across the channel. The biasing scheme in Fig. 2(c) corresponds to the THz voltage induced between the source and drain resulting in the terahertz drain current. Our simulation reveals the contact effects and the appearance of low frequency modes propagating in the entire structure in contrast to the plasmonic excitations under the individual gate fingers. These results are important for the design, optimization, compact modeling, and parameter extraction of the ratchet plasmonic sub-THz and THz detectors.

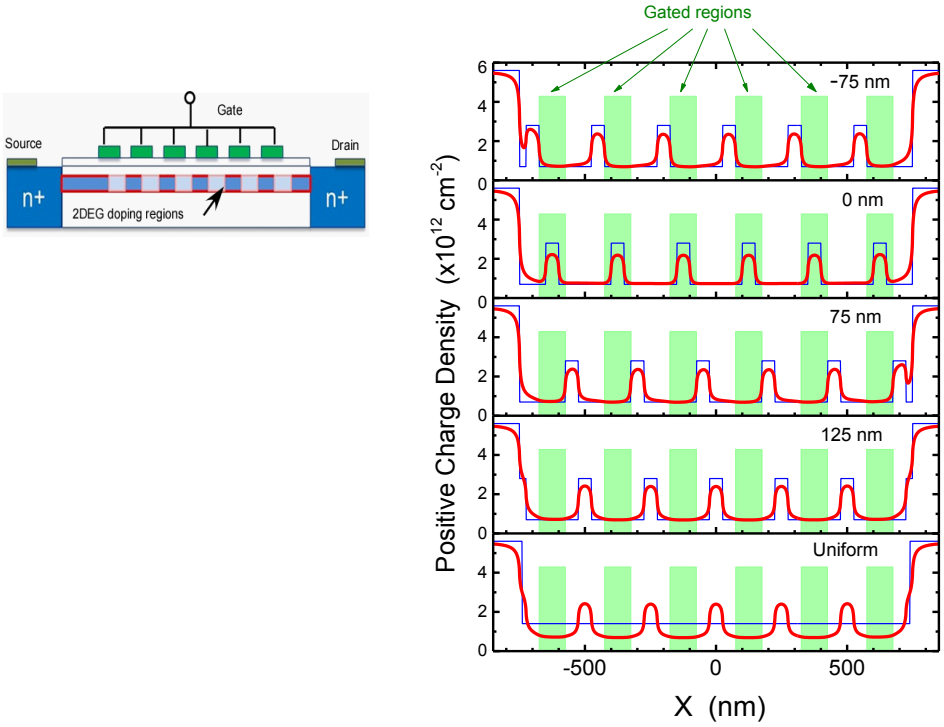

(a) (b)

FIG. 1 (a) Multi-finger 2DEG ratchet structure. (b) Four upper panels: modulated positive charge density (thin lines) in the channel offset with respect to the gate. The gated regions are shaded in the figure. The base donor sheet charge density is 0.7×10^{16} m^{-2}; the high donor sheet charge density is 2.8×10^{16} m^{-2}. Contact regions sheet charge density 5.6×10^{16} m^{-2}. Numbers show the shift of the high modulating charge with respect to the finger position. Computed electron density distributions are shown in red (color on-line). The lowest panel is for the case of the uniform doping density between the highly doped contact regions. The gate-to-source voltage $V_{gs} = -0.3$V, higher than the single gate threshold voltage which was estimated to be about -0.5V.

—

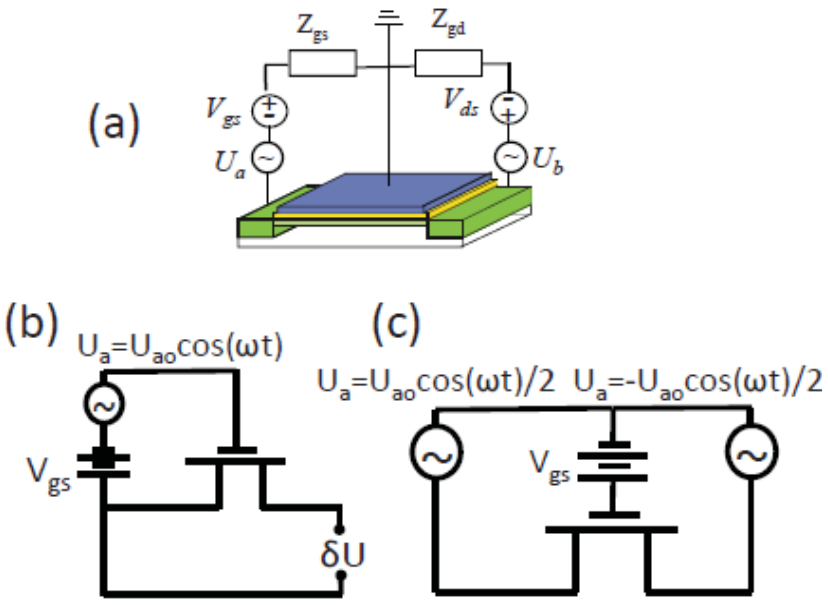

FIG. 2. (a) General biasing scheme with two AC inputs and two impedances. Simpler biasing arrangements used in the simulation: (b) THz voltage is induced between the source and gate with the open drain circuit ($Z_{gd} = \infty$), (c) THz voltage induced between the source and drain resulting in the terahertz drain current ($U_b = U_a$, $Z_{gs}=Z_{gd}$).

Equations and boundary conditions.

Here we will describe our hydrodynamic model[21]. The model equations are the continuity equation:

$$\frac{\partial n}{\partial t} + \nabla \cdot (n\boldsymbol{u}) = 0, \tag{1}$$

the Navier-Stokes equation

$$\frac{\partial \boldsymbol{u}}{\partial t} + (\boldsymbol{u}\cdot\nabla)\boldsymbol{u} + \frac{e}{m}\nabla U + \frac{1}{n}\nabla P + \frac{\boldsymbol{u}}{\tau} - \nu\nabla^2\boldsymbol{u} = 0, \tag{2}$$

and the energy balance equation relating electron temperature and hydrodynamic velocity[21]. For small signals the temperature variation across the device is relatively small and the energy balance equation is not included in our simulations for this paper. Here n is the 2DEG density, $\boldsymbol{u}$ is the 2D hydrodynamic (or drift) velocity, m is the electron effective mass, ν is the kinematic viscosity coefficient, U is the channel potential, P is pressure, $\tau = \mu m/e$ is the momentum relaxation time, and μ is electron mobility in the channel.

To the order in which the hydrodynamic model is derived from the quasi-classical Boltzmann equation, the pressure P and the internal energy per electron Σ at temperature T are given by

$$P = \frac{n\Sigma}{m} = \frac{nk_B TF_1(\xi)}{F_0(\xi)}, \quad (3)$$

where ξ is the chemical potential in units of k_BT: $\xi = ln[exp(E_F/k_BT) - 1]$ and Fermi energy $E_F = \pi\hbar^2 n/m$. $F_n(\xi)$ is the Fermi integral, defined as

$$F_m(y) = \int_0^\infty dx \frac{x^m}{1 + \exp(x - y)}. \quad (4)$$

The analysis of hydrodynamic equations using the unified charge control model for a single finger gate was reported in reference 21. Here we solve hydrodynamic equations coupled to the Poisson equation. An estimate of viscosity for electrons in a gated channel can be obtained using the low temperature approximation[22]:

$$\nu \approx \frac{2\hbar}{\pi m} \frac{T_F^2}{T^2} \frac{1}{ln\left(\frac{2T_F}{T}\right)} \quad (5)$$

where T_F is the Fermi temperature and □ is Plank's constant. For the simulated structure with an approximate density of 7.5×10^{11} cm^{-2} T_F = 510 K and the effective electron mass m=0.041m_o, we obtain $\nu \approx 42.4$ cm^2/s.

To calculate the electric potential in the channel, we used the simplified device geometry (shown in the inset of Fig. 4a) where the source and the drain contacts are in the same plane as the channel, and the source, drain and gate contacts are infinitely thin. The source, drain and gate are assumed to be ideal conductors with a constant voltage across the metal. For our simplified geometry, the charge from the ionized donors is also assumed to be in the plane of the channel. In our calculation, we do not account for the effect of the chemical potential on the difference between the voltage applied between the source and the gate (or drain and gate) and the electric potential. This can lead to a small artificial voltage between source and drain in the case of the scheme shown in Fig. 2b, and a small current in the case of the case of the scheme shown in Fig. 2c, when no THz signal is applied. This voltage or current is subtracted out of the results when a THz signal is applied. The electric potential and the charge distribution in the channel and contacts are related through the Poisson equation, in SI units:

$$\frac{\partial^2 U}{\partial x^2} + \frac{\partial^2 U}{\partial^2 y} + \frac{\partial^2 U}{\partial x^2 z} = \frac{e}{\varepsilon_s \varepsilon_0} n_T(x, y)\delta(z), \quad (6)$$

where $-L_s - L/2 < x < L/2 + L_d$, L is the length of the channel, L_s and L_d are lengths of the source and drain metal contacts, respectively, e is the absolute value of the electron charge, ε_s is the dielectric permittivity, and ε_0 is the dielectric permittivity of vacuum . In the channel the total charge density is related to the electron density $n(x,y)$ in Eq. (1) by

$$n_T(x, y) = n(x, y) - N^+_{donor}(x, y), \quad |x| < L/2 \quad (7)$$

where N^{+}_{donor} is the density of the donors in the channel plane, see Fig. 1(b).

The simulations were performed for two types of the boundary conditions. The boundary conditions for the detector with the voltage output, Fig. 2(b), used in the simulation are

$$U(x=-L/2)=U_{a0}\cos(\omega t)+V_{gs} \tag{8a}$$

$$\frac{\partial Q_{drain}}{\partial t}=-en(x=L/2)u(x=L/2)W \tag{8b}$$

$$\left.\frac{\partial^2 u}{\partial x^2}\right|_{x=\pm L/2}=0 \tag{8c}$$

where W is the width of the device. Q_{drain} is the total charge on the drain contact obtained by solving the Poisson equation for the electric potential with the Eq. (8b), and determines the voltage at the drain contact. Eq. (8b) describes continuity of current at the interface of the channel and the drain contact. The boundary conditions for the detector with the rectified drain current output, Fig. 2c, are

$$U(x=-L/2)=U_{a0}\cos(\omega t)/2+V_{gs} \tag{9a}$$

$$U(x=L/2)=-U_{a0}\cos(\omega t)/2+V_{gs} \tag{9b}$$

and Eq. (8c).

Rozhansky et. al.[18] showed that a phase shift between a static periodic device potential and a spatially periodic impinging THz field can result in a significant increase in the device response. The analysis of ref. 18 was based on a space-harmonic electric potentials in an infinitely long device. In our device the THz field is applied between the gate and the source (and the drain in the case of the current output device) similar to the original work of Dyakonov and Shur[11] . In addition, our device has a finite number of gate fingers and we directly calculate the resulting potentials self-consistently. Fig. 3 shows the static potential due to the periodic doping, and the envelope of the induced terahertz electric field for our device. It can be seen that the majority of the induced electric field is between the first gate and the source (and the last gate and the drain in the current output device). A small periodic electric field is induced and the phase shift between the envelope of the THz signal and the static device potential can be controlled in the device fabrication[23].

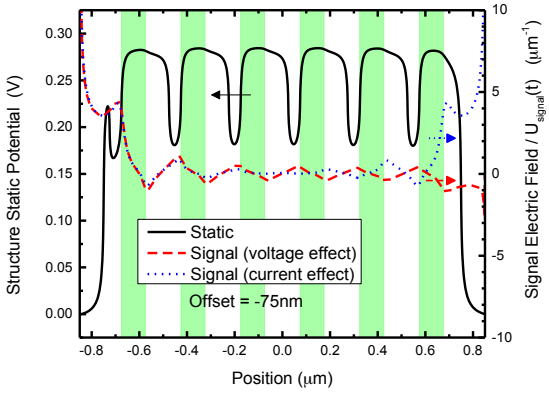

FIG. 3: Static potential due to the periodic doping (black line), and the envelope of the induced terahertz electric field for the device with a voltage output (dashed red line) and the device with a current output (dotted blue line) (color on-line).

Table 1 lists the parameters used in the simulation. Most of these parameters came from the Semiconductor Parameter Handbook[24] with the rest given in Reference 21.

Table 1. Parameters used in the simulation.

Parameter	Value	Unit
Effective mass	0.041	
Mobility	3500 to 40000	cm^2/Vs
Threshold voltage	-0.5	V
Viscosity	42. 5	cm^2/s
Lattice temperature	300	K
Device width	10	μm
Source-to-drain separation	1.7	μm
Gate finger separation	150	nm
Gate finger length	100	nm
Barrier layer thickness	20.4	nm
Dielectric permittivity	13.9	-

RESULTS AND DISCUSSION

Fig. 4(a) shows the DC voltage change between source and drain induced by the THz signal for biasing scheme of Fig. 2(b) for different values of the channel modulation placement with respect to the gate fingers, with a channel mobility of 3500 cm^2/Vs. Fig. 4(b) shows the output drain current induced by the THz signal for biasing scheme of Fig. 2(c). For the current output device (Fig. 4b), the doping offsets of 0 nm or 125 nm result in a device that is completely symmetric, with the THz harmonic field being completely anti-symmetric. In this case, there is no distinction between the source and the drain, and the current must be zero. (A small numerical

error can be seen in our calculation at high frequency.) The sign of the DC current is determined by the sign of the offset position.

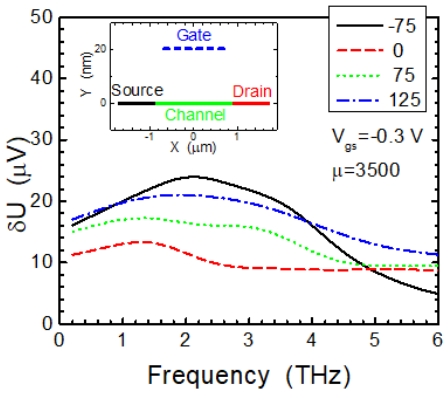

(a)

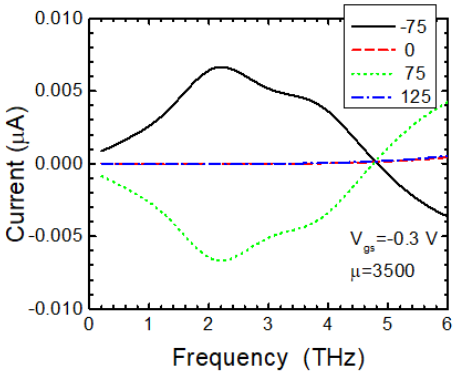

(b)

FIG. 4. (a) DC voltage change between source and drain induced by the THz signal (negative of drain-to source voltage) for biasing scheme of Fig. 2(b). (b) Drain current induced by the THz signal (for biasing scheme of Fig. 2(c). The input signal amplitude 5 mV. The numbers in the legends are the offsets of the highly doped regions with respect to the gate fingers (in nm) shown in Fig. 1(a). The electron channel mobility is 3500 cm^2/Vs, the gate finger length is 100 nm, and the ungated section length is 150 nm. The inset shows simplified device geometry used in our model.

In order to distinguish individual resonances and better understand the results, we also show the response for a detector with high mobility of 40000 cm^2/Vs in Fig. 5, for the two biasing schemes. Such high mobility may be possible at cryogenic temperatures.

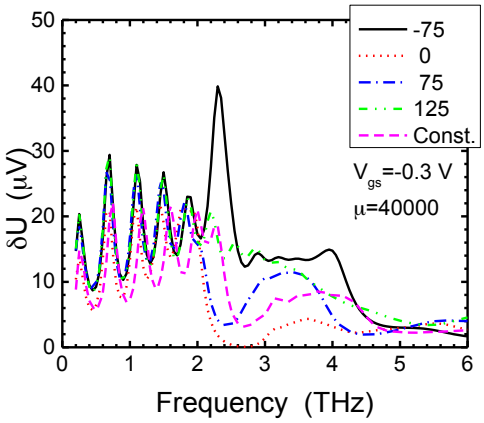

(a)

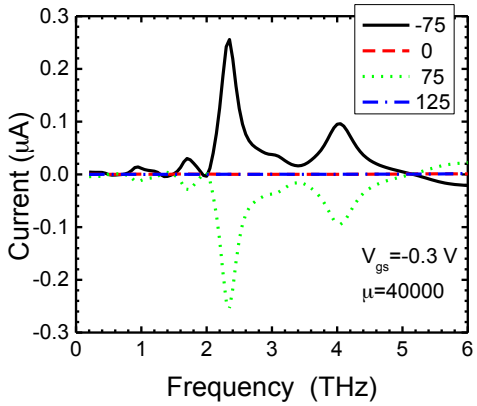

(b)

FIG. 5. (a) DC voltage change between source and drain induced by the THz signal for biasing scheme of Fig. 2(b) for the high mobility case, μ = 40000 cm^2/Vs, dashed line shows response of the InGaAs HEMT with uniform doping 1.4×10^{12} cm^{-2}. (b) Drain current induced by the THz signal for biasing scheme of Fig. 2(c). The numbers in the insets are the offsets of the highly doped regions with respect to the gate fingers (in nm).

Both boundary conditions show a large peak around a frequency of 2.32 THz. An analytical approximation for the frequency of this peak can be obtained from plasma velocities s_g and s_{ug} corresponding to the gated and ungated sections of lengths L_g and L_{ug}, correspondingly:

$$f_p = \frac{1}{2\left(\frac{s_{ug}}{L_{ug}} + \frac{s_g}{L_g}\right)} \quad . \tag{10}$$

The velocities are given by

$$s_{ug} = \sqrt{e^2 n / 2\varepsilon_0 \varepsilon_s q m}\,, \tag{11}$$

where we set $q = \pi/(L_{ug} + L_g)$, assuming that we have a half wave per period, and

$$s_g = \sqrt{\frac{\eta k_B T}{m} \ln\left(1 + e^{eU_0/\eta k_B T}\right)\left(1 + e^{-eU_0/\eta k_B T}\right)} \quad , \tag{12}$$

where η is a non-ideality factor[21] and U_0 is the gate voltage above the threshold, $U_0 = U_g - U_t$. For $U_0 > 0$ the plasma velocity in the gated section can be approximated as $s_g \approx \sqrt{eU_0/m}$, while for $U_0 < 0$ $s_g \approx \sqrt{\eta k_B T/m}$. In this analytical approximation we ignored the change in U_0 due to the doping density changing the effective threshold voltage, ignored the edge effects, assumed that L_g is much larger than the gate to channel distance, and did not include pressure effects and effect of the transition regions between gated and ungated sections. Fig. 6 shows the drain current for the current output device for three different values of the lengths of the gated and ungated sections. The resonant values obtained from the analytical approximation of Eq. (10) are indicated in the figure. For the three cases of L_g = 100 nm and L_{ug} = 150 nm, L_g = 100 and L_{ug} = 300 nm, L_g = 200 nm and L_{ug} = 150 nm, Eq. (10) gives f_p = 2.23 THz, 1.47 THz, and 1.51 THz, correspondingly. As seen in Fig. 6, these values are within a few percent of the numerically computed resonant frequencies.

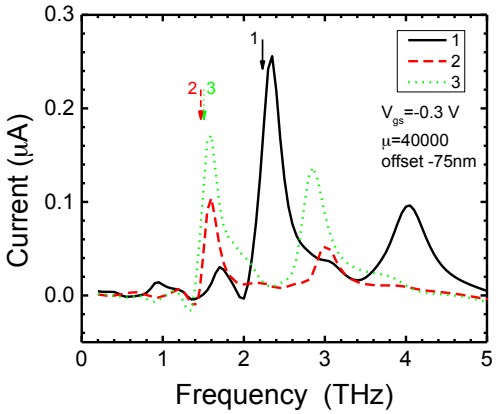

FIG. 6. Drain current induced by a terahertz signal for the biasing scheme of Fig. 2c for three different devices. For each device an arrow shows the estimated fundamental peak frequency. For the device # 1 L_g =100 nm and L_{ug}=150 nm, for the device # 2 L_g =100 nm and L_{ug} =300 nm, for the device # 3 L_g =200 nm and L_{ug} =150 nm.

The asymmetry induced by the ratchet modulation enables the rectification of the drain to source THz voltage. When the THz radiation couples to the device via the interconnect wiring or specially designed antennas, generally speaking, the THz voltages are induced between the source and gate and source and drain[25] (see Fig. 2(a), which is similar to Fig. 1(c) from ref. 25). We label these THz signal induced voltages U_a and U_b, with the amplitudes U_{a0} and U_{b0} respectively. In the case of small signals, when U_{a0} and U_{b0} are small compared to the gate voltage swing $U_0 > 0$, using perturbation analysis[11] it is possible to obtain an analytical approximation for the induced DC voltage. The resulting response U_{DC} for the collision dominated case (low mobility) for a long symmetrical device and open circuit boundary conditions at the drain is given by[26]

$$U_{DC} = -\frac{U_{ao}^2 - U_{bo}^2}{4U_o} \quad . \tag{13}$$

Eq. (13) is valid for small AC signals above threshold. For a short symmetrical device, the response depends on the phase difference θ between $U_a = U_{ao}\sin(\omega t)$ and $U_b = U_{bo}\sin(\omega t + \theta)$ [27]

$$U_{DC} = -\alpha\left(\left|U_{ao}^2\right| - \left|U_{bo}^2\right|\right) - \beta U_{ao}U_{bo}\sin\theta \quad . \tag{14}$$

Parameters α and β are complicated functions of the gate length and load and input impedances. Whereas for a symmetrical device the value of β is determined by the difference between the impedances Z_{gs} and Z_{gd}, this coefficient is determined by the internal asymmetry of the ratchet

device and the response $U_{DC} = I_{DS} R_{DS}$, where I_{DS} and R_{DS} are the calculated drain-to-source DC current (for the biasing scheme of Fig. 2(c)) and drain-to-source DC resistance, respectively.

As was discussed in the references 11 and 21, the electron viscosity plays an important role contributing to the plasmon attenuation. The effect of viscosity is shown in Fig. 7 and Fig. 8 for the case of the current output device for two different lengths of the gate finger, for low and high mobility cases, respectively.

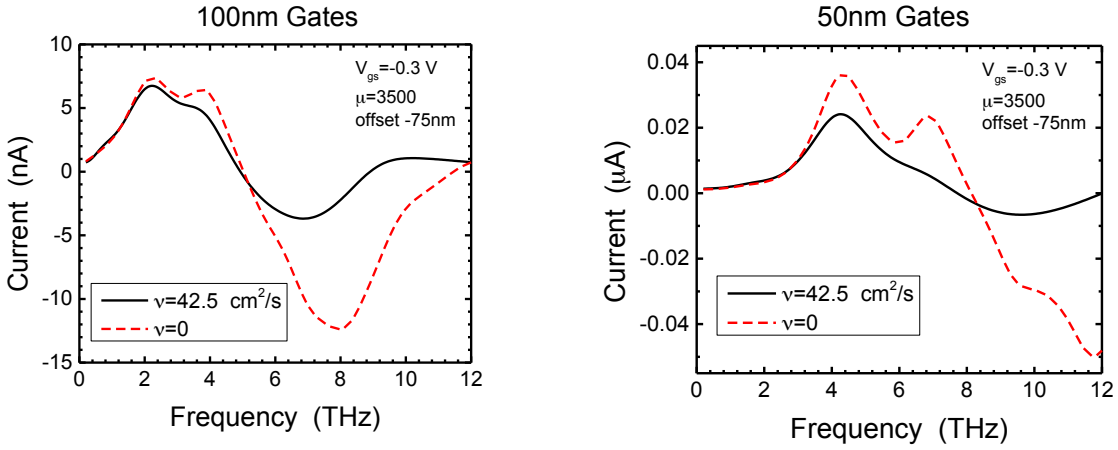

(a) (b)

FIG. 7. Drain current induced by the THz signal for the detector biasing scheme of Figure 2(c) for the electron mobility 3500 cm^2/Vs with and without viscosity effect, for two different gate finger lengths.

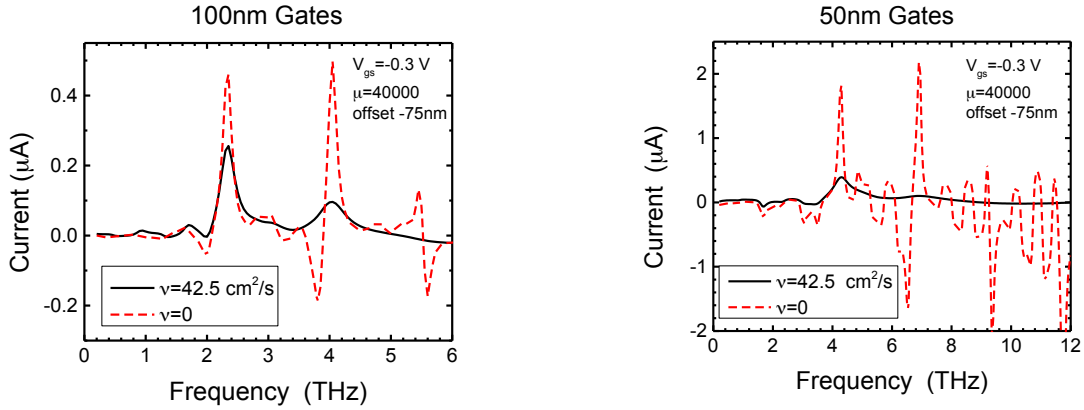

(a) (b)

FIG. 8. Drain current induced by the THz signal for the detector biasing scheme of Figure 2(c) for the electron mobility 40000 cm^2/Vs with and without viscosity effect, for two different gate finger lengths.

As seen from Fig. 8, the viscosity has noticeable effect at the plasmonic maximum at around 2.5 THz for the 100 nm devices and dominant effect at all plasmonic maxima for the 50 nm device and for the 100 nm device above 3 THz. Viscosity has only a limited effect in the low mobility structures, see Fig. 7. For a qualitative estimate of the gate finger length for where the viscosity

starts playing a role we can use the plasmon dispersion relation between frequency ω and wave-vector k obtained in the linear approximation of the hydrodynamic equations[21] :

$$\omega^2 + i\omega/\tau - k^2\left(s^2 - i\nu\omega\right) = 0. \qquad (15)$$

The viscosity effect becomes important when the momentum relaxation $1/\tau$ is equal to the viscosity damping νk^2. For the plasmon wavelength equal to $2L$ the viscosity effect is significant for the gate finger length on the order of $L < L_{cr} = \sqrt{\pi^2\nu\tau} = \sqrt{\pi^2 \nu m\mu/e}$. This gives L_{cr} = 58nm for the electron mobility μ = 3500 cm^2/Vs and L_{cr} = 198 nm for μ = 40000 cm^2/Vs.

The simulation results reveal two new features of the THz response. First, the new feature (not revealed by the analytical model[18]) is that the THz induced rectified current changes sign at high frequency. This change occurs at the frequency at which the phase shift due to the plasma wave propagation along the offset distance $\Delta\varphi = \omega\Delta x/s$ is equal to $n\pi$. Here Δx is the offset of the ratchet structure (see Fig. 1). As seen from figures 4 - 7 this frequency is nearly 4.5 THz and 9 THz independently of the low field mobility. This change in sign could be interpreted as the phase shift of the plasma wave propagating in the region between the gated and modulated electron density regions. The sign changes when

$$f_{sign} = \frac{s}{2\Delta x} \quad . \qquad (16)$$

Here f_{sign} is the frequency at which the rectified current changes sign. Measuring this frequency should allow for accurate plasma velocity extraction.

Another important feature is merging of the plasmons in the gated and ungated sections of the channel and the appearance of the plasmonic maxima at lower frequencies (see Fig. 5a). These peaks occur at high values of the low field mobility. The analytical model did not predict these peaks because it was considering an infinite number of the identical cells of the ratchet plasmonic crystal. The wave-forms of the propagating plasma waves can be seen by plotting current as a function of position at different times. In Fig. 9 the current as a function of position along the 100 nm gate finger current output device (Fig. 2c) is shown at instances separated by time intervals of one tenth of the period 1/f, for four resonant frequencies.

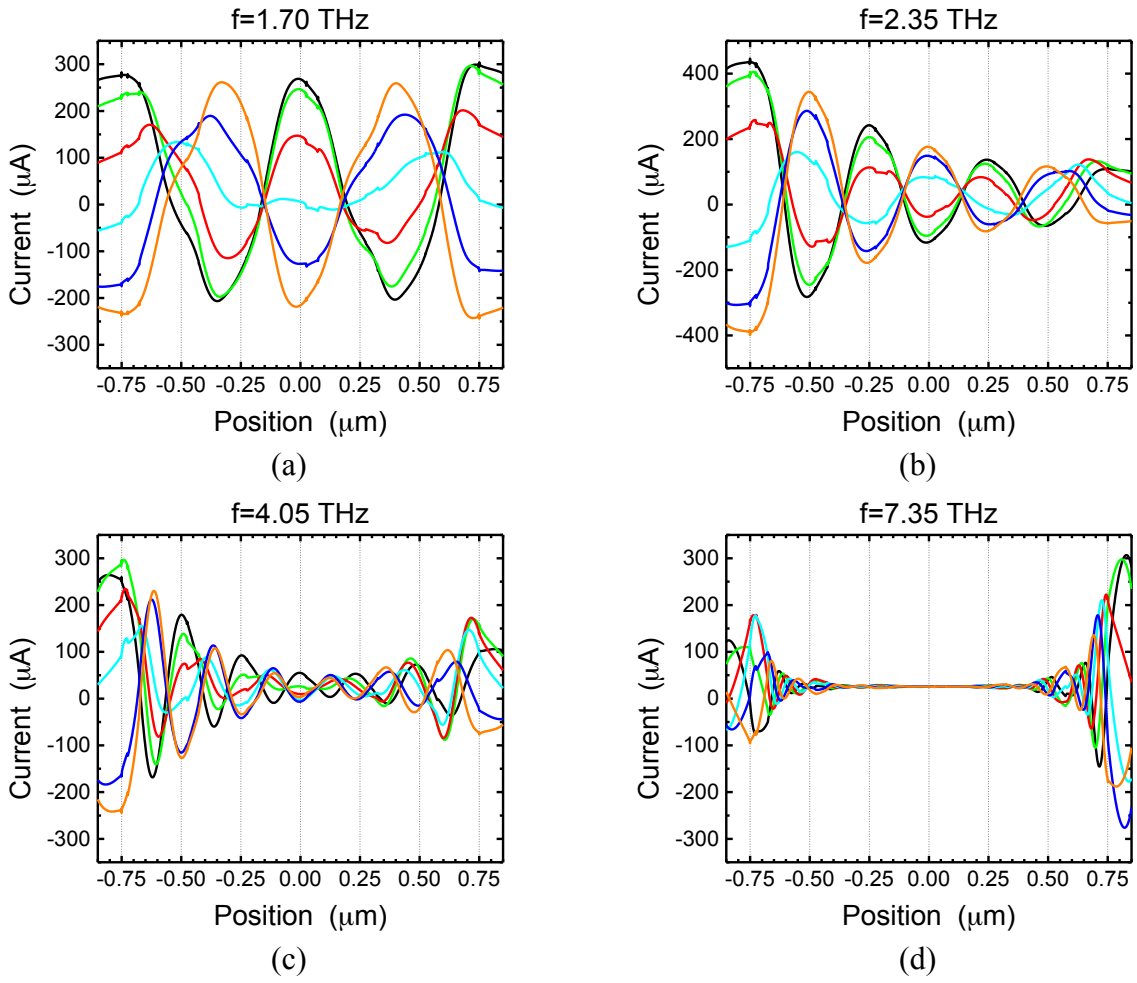

FIG. 9. Current profiles at different frequencies. The lines correspond to time instances separated by 0.1*f*. The time sequence is indicated by the color (on-line): black, green, red, cyan, blue, and orange.

While the resonant wave at $f = 2.35$ THz can be described as a plasma resonance of the single gate finger half-wave device, Eq. (10), in general the interpretation of the oscillations require the modeling of the whole multi-finger device. At lower frequencies, figures 9a-9c, the plasma wave propagates through the device, while at higher frequencies, Fig. 9d, the oscillations are viscosity damped and confined to the regions of the end fingers.

CONCLUSIONS.

The hydrodynamic simulations confirm the appearance of the plasmonic peaks at the fundamental frequency of the gated plasmons in the ratchet structures with a finite number of the gate fingers. But these simulations also reveal the appearance of lower frequency plasmonic peaks with the wavelengths determined by the overall device length. In the analytical theory of the infinite plasmonic ratchet structures, such peaks degenerate into a zero frequency response peak. The built-in asymmetry of the ratchet structures allows for the drain to source current

response to the THz signal applied between the source and drain contacts. In the symmetrical structures, a similar response could be induced by the applied DC current breaking the symmetry. We found that the frequency of the main resonance can be approximated by a simple analytical formula for a junction of one gated and one ungated sections of the channel, while the frequencies of other resonances have to be obtained from numerical solution for the whole multi-fingered structure. The ratchet structure asymmetry can enhance the response beyond conventional grating gate structure, when the ratchet response add constructively with the conventional response. Even in relatively low mobility structures, the enhancement is about a factor of 2 or 3. The ratchet structures operating in the resonance plasmonic regime are the plasmonic THz detectors with the highest responsivity. The ratchet response is strongly dependent on how the THz radiation is coupled to the structure. For coupling that applies the THz voltage between the drain and source, the shape of the response dependence on frequency changes dramatically, primarily a viscosity damping effect. The analytical model developed in ref. 18 predicted large plasmonic peaks for both lateral and longitudinal current components but did not account for the viscosity, ν , of the electronic fluid, which causes an additional dissipation rate [11] on the order of νk^2, where $k \sim 2\pi/L_g$ is the plasmon wave vector and L_g is the gate finger length (the exact relationship between k and L depends on the boundary conditions). The response exhibits a plasmonic peak with half width determined by impurity and phonon scattering and by the viscosity of the electronic fluid. At high frequencies, high mobilities, and short feature sizes (on the order of 50 nm) viscosity becomes a dominant attenuation mechanism. This must be accounted for in the design of sub-THz, THz, and far infrared devices.

ACKNOWLEDGMENT

The work at RPI was supported by the US ARL Cooperative Research Agreement (Project Monitor Dr. Meredith Reed) and by US Army Research Office (Project Monitor Dr. Joe Qiu).

REFERENCES

[1] I. Kallfass, F. Boes, T. Messinger, et al., 64 Gbit/s transmission over 850 m fixed wireless link at 240 GHz carrier frequency, J. Infrared, Millimeter, and Terahertz Waves, **36**, no. 2, pp. 221-233 (2015).

[2] W. R. Deal, T. Foster, M. B. Wong, M. Dion, K. Leong, X. B. Mei, A. Zamora, G. Altvater, K. Kanemori, L. Christen, J. C. Tucek, M. A. Basten, and K. E. Kreischer, A 666 GHz Demonstration Crosslink with 9.5 Gbps Data Rate, in 2017 IEEE MTT-S International Microwave Symposium (2017).

[3] J. Federici and L. Moeller, Review of terahertz and subterahertz wireless communications, J. Appl. Phys. **107**, 111101 (2010); doi: 10.1063/1.3386413

[4] K. Kamburoglu and N. Yetimoğlu, Applications of Terahertz Imaging in Medicine, OMICS J. Radiol. **3**, e127 (2014). doi: 10.4172/2167-7964.1000e127

[5] C. Yu, Sh. Fan, Y. Sun, and E. Pickwell-MacPherson, The potential of terahertz imaging for cancer diagnosis: A review of investigations to date, Quant. Imaging Med. Surg. **2**(1), 33 (2012). doi: 10.3978/j.issn.2223-4292.2012.01.04

[6] S. Rumyantsev, A. Muraviev, S. Rudin, G. Rupper, M. Reed, J. Suarez and M. Shur, Terahertz Beam Testing of Millimeter Wave Monolithic Integrated Circuits, IEEE Sensors J. **17**, no. 17, 5487 (2017) .

[7] W. Stillman, D. Veksler, T. A. Elkhatib, K. Salama, F. Guarin, and M. S. Shur, Sub-terahertz testing of silicon MOSFET, Electron. Lett. **44**, no. 22, pp. 1325–1327(2008).

[8] H. Zhong, N. Karpowicz, J. Xu, YA. Deng, W. Ussery, M. Shur, X.-C. Zhang, Inspection of space shuttle insulation foam defects using A. 0.2 THz Gunn diode oscillator, Infrared and Millimeter Waves, 2004 and 12th International Conference on Terahertz Electronics, Conference Digest of the 2004 Joint 29th International Conference, pp.753-754 ISSN: DOI: 10.1109/ICIMW.2004.1422311

[9] Y. Chen, H. Liu, Haibo; M. J. Fitch, Rosined, J. B. Spicer, M. S. Shur, X. C. Zhang, THz diffuse reflectance spectra of selected explosives and related compounds, Passive Millimeter-Wave Imaging Technology VIII. Edited by Appleby, Roger; Wikner, David A. Proceedings of the SPIE, Vol. 5790, pp. 19-24 (2005).

[10] M. S. Shur, Terahertz Electronics for Sensing and Imaging Applications, Proc. SPIE 9467, Micro- and Nanotechnology Sensors, Systems, and Applications VII, 94672A (May 22, 2015); doi:10.1117/12.2085442

[11] M. I. Dyakonov and M. S. Shur, Plasma wave electronics: novel terahertz devices using two dimensional electron fluid, IEEE Trans. ED, **43**, no. 10, pp. 1640-1646, (1996).

[12] T. Otsuji and M. Shur, Terahertz Plasmonics: Good results and great expectations, IEEE Microwave Journal **15**, no.7, 43 (2014).

[13] M. S. Shur, V. Ryzhii, and R. Gaska, Method of generation and manipulation of terahertz and microwave radiation, filed 10/29/03, US Patent 7,955,882.

[14] A. S. Petrov, D .Svintsov, V. Ryzhii and M. S. Shur, Amplified-reflection plasmon instabilities in grating-gate plasmonic crystals, Phys. Rev. **B** 95, 045405 (2017).

[15] M. Karabiyik, A. Ahmadivand, R. Sinha, C. Al-Amin, P. K. Vabbina, S. Kaya, G. Rupper, S. Rudin, M. Shur and N. Pala, Plasmonic properties of asymmetric dual grating gate plasmonic crystals, physica status solidi (b) Volume 253, no. 4, pp. 671–675 (2016) DOI: 10.1002/pssb.201552609.

[16] V. V. Popov, D. V. Fateev, O. V. Polischuk, M. S. Shur, Optics Express, Enhanced electromagnetic coupling between terahertz radiation and plasmons in a grating-gate transistor structure on membrane substrate, **18**(16):16771-6 (2010).

[17] A. V. Muravjov, D. B. Veksler, V. V. Popov, O. Polischuk, X. Hu, R. Gaska, N. Pala, H. Saxena, R. E. Peale, M. S. Shur, Temperature dependence of plasmonic terahertz absorption in grating-gate GaN HEMT structures, Appl. Physics Lett **96**, 042105 (2010).

[18] I. V. Rozhansky, V. Yu. Kachorovskii, and M. S. Shur, Helicity-Driven Ratchet Effect Enhanced by Plasmons, Phys. Rev. Lett. **114**, 246601 (2015).

[19] P. Olbrich, J. Kamann, M. König, J. Munzert, L. Tutsch, J. Eroms, D. Weiss, Ming-Hao Liu, L. E. Golub, E. L. Ivchenko, V. V. Popov, D. V. Fateev, K. V. Mashinsky, F. Fromm, Th. Seyller, and S. D. Ganichev, Terahertz ratchet effects in graphene with a lateral superlattice, Phys. Rev. B **93**, 075422, (2016).

[20] S. D. Ganichev, D. Weiss, J. Eroms, Terahertz Electric Field Driven Electric Currents and Ratchet Effects in Graphene, Annalen der Physik **529**, 1600406 (2017). DOI: 10.1002/andp.201600406

[21] S. Rudin, G. Rupper, A. Gutin, and M. Shur, Theory and measurement of plasmonic terahertz detector response to large signals, J. Appl. Phys. **115**, 064503 (2014); DOI: 10.1063/1.4862808

[22] S. Rudin, Temperature dependence of the non-linear plasma resonance in gated two-dimensional semiconductor conduction channels, Appl. Phys. Lett. **96**, 252101 (2010).

[23] In future work, we would like to simulate the effect of the THz signal impinging directly onto the device. This would most likely lead to a much larger periodic envelope while reducing the edge effects.

[24] M. E. Levinshtein, S. Rumyantsev, and M. S. Shur, Editors, Handbook of Semiconductor Material Parameters, Vol. 2, Ternary and Quaternary III-V compounds, World Scientific, ISBN 981-02-1420-0 (1999).

[25] J.-Q. Lu, M. S. Shur, J. L. Hesler, L. Sun, and R. Weikle II, A Resonant Terahertz. Detector Utilizing a High Electron Mobility Transistor, IEDM Technical Digest, pp. 453-456, San Francisco, CA (1998).

[26] D. B. Veksler, A.V. Muravjov, V. Yu. Kachorovskii, T. A. Elkhatib, K. N. Salama, X.-C. Zhang and M. S. Shur, Imaging of field-effect transistors by focused terahertz radiation, Solid-State Electronics **53**, Issue 6, pp. 571-573(2009).

[27] K. S. Romanov and M. I. Dyakonov, Theory of helicity-sensitive terahertz radiation detection by field effect transistors, Appl. Phys. Lett. **102**, 153502 (2013).